AGU PUBLICATIONS

JGR

Journal of Geophysical Research: Oceans

RESEARCH ARTICLE

10.1002/2013JC009270

Key Points:
- Structure and variability of the alongshore coastal currents off southern Peru
- Impact of a coastal-trapped wave on the near-coastal circulation off Peru

Correspondence to:
A. Pietri,
alice.pietri@locean-ipsl.upmc.fr

Citation:
Pietri, A., V. Echevin, P. Testor, A. Chaigneau, L. Mortier, C. Grados, and A. Albert (2014), Impact of a coastal-trapped wave on the near-coastal circulation of the Peru upwelling system from glider data, *J. Geophys. Res. Oceans*, *119*, 2109–2120, doi:10.1002/2013JC009270.

Received 11 JULY 2013
Accepted 27 FEB 2014
Accepted article online 8 MAR 2014
Published online 26 MAR 2014
Corrected 22 MAY 2014

This article was corrected on 22 MAY 2014. See the end of the full text for details.

Impact of a coastal-trapped wave on the near-coastal circulation of the Peru upwelling system from glider data

Alice Pietri[1], Vincent Echevin[1], Pierre Testor[1], Alexis Chaigneau[2], Laurent Mortier[1], Carmen Grados[3], and Aurélie Albert[1]

[1]LOCEAN-IPSL, Paris, France, [2]LEGOS-OMP, Toulouse, France, [3]IMARPE, Callao, Lima, Peru

Abstract Geostrophic alongshore velocity data from a glider repetitive section off the coast of Peru (14°S) are used to study the cross-shore structure and temporal variability of the Peru current system during a 5 week period in April–May 2010. Besides providing substantial information on the surface frontal jet associated with the Peru Coastal Current and the surfacing Peru-Chile Undercurrent that flows poleward trapped on the continental shelf and slope, the glider data reveal the presence of an intense deep equatorward current, which transports up to ∼2.5 Sv. The dynamics of this current are investigated using an eddy-resolving regional model. The variability of the vertically sheared alongshore flow is shown to be related to the passage of a poleward propagating coastal-trapped wave likely of equatorial origin. Solutions from a two-dimensional, linear, coastal wave model suggest that the alongshore current observed vertical structure is associated with the second and third baroclinic modes of the coastal-trapped wave.

1. Introduction

The Peru Current System (PCS) is the northern part of the South Pacific Ocean eastern boundary current system. It is characterized by permanent coastal upwelling driven by the sustained atmospheric wind jet formed by the eastern limb of the South Eastern Pacific Subtropical Anticyclone [*Strub et al*., 1998] and mainly composed of an equatorward surface current, the Peru Coastal Current (PCC), and a poleward undercurrent, the Peru-Chile Under Current (PCUC). The PCC flows alongshore at a speed of ∼15 cm s^{-1} and has a vertical extent of ∼50 m [*Huyer et al*., 1991]. On the shelf, it is primarily driven by the surface wind [*Wyrtki*, 1966, 1967] and reinforced by the cross-shore pressure gradient induced by the density difference between the newly upwelled cool coastal waters and the warmer offshore waters. The PCUC, centered at around 100 m depth in the Peru region, flows poleward along the continental shelf and upper slope at a speed of ∼20 cm s^{-1} and has a typical vertical extent of 300–400 m [*Huyer*, 1980; *Chaigneau et al*., 2013]. The mechanisms forcing this current are not completely clear: it is partly forced by the nearshore negative wind stress curl generating a poleward transport through Sverdrup dynamics [e.g., *Marchesiello et al*., 2003; *Albert et al*., 2010; *Chaigneau et al*., 2013] but other processes involving alongshore density gradients and remotely forced coastal waves also play a role [*Echevin et al*., 2011]. The upwelling system associated currents are subject to important intraseasonal variability due to local and remote forcing: they are influenced by alongshore winds [*Hormazabal et al*., 2001; *Dewitte et al*., 2011] and by coastal-trapped waves (CTW) of equatorial origin [*Brink*, 1982; *Romea and Smith*, 1983; *Hormazabal et al*., 2002], which can be forced by the Intraseasonal Equatorial Kelvin Waves (IEKW) [e.g., *Cravatte et al*., 2003] reaching the coasts of South America. In particular, previous studies have shown that the PCUC is modulated by intraseasonal variability associated with CTW [*Brink et al*., 1978; *Shaffer et al*., 1997]. Although the near-surface (∼0–500 m) PCS has been relatively well documented [*Brink et al*., 1983; *Huyer et al*., 1991; *Strub et al*., 1998], the nearshore circulation below the undercurrent is not well known. In a recent study, *Chaigneau et al*. [2013] reported the presence of an equatorward flow off Peru located below the PCUC, the Chile-Peru Deep Coastal Current (CPDCC). Further South, at 30°S off the Chilean coast, *Shaffer et al*. [1997] also reported evidence of equatorward deep flow. These results are consistent with model simulations which show a relatively intense deep equatorward flow (∼5–10 cm s^{-1}) during the peaking phase of El Niño events [*Colas et al*., 2008; *Montes et al*., 2011] and a weaker amplitude (∼2 cm s^{-1}) at annual time scale [*Montes et al*., 2010].

In this paper, we document the cross shore and vertical structure of the alongshore coastal currents off southern Peru (near Pisco, 14°S) using in situ glider measurements acquired along a repetitive cross-shore

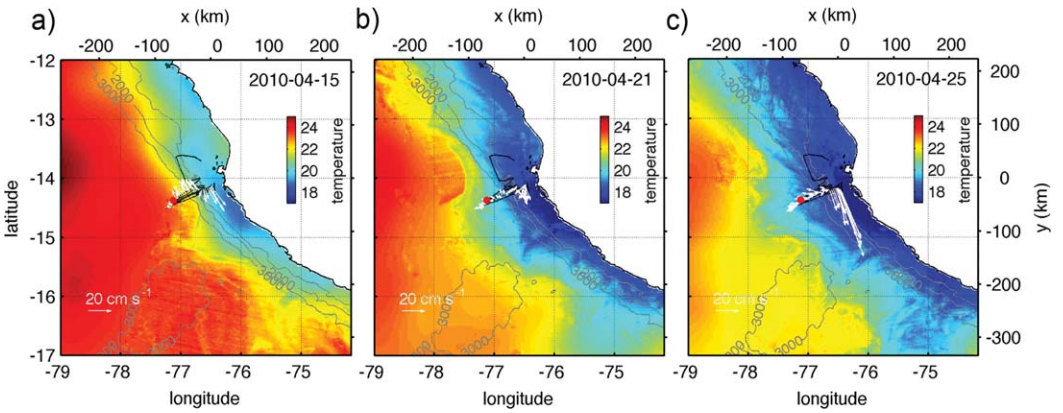

Figure 1. MODIS sea surface temperature on (a) 15 April 2010, (b) 21 April 2010, and (c) 25 April 2010 in the Peru upwelling region. Black lines represent the glider trajectories and white arrows the depth integrated velocity from (a) 14 to 19 April, (b) 19 to 23 April, and (c) 23 to 28 April. Red dot indicates the data point where the wind stress was plotted (see Figure 2).

section occupied between the surface and 1000 m depth. The glider deployment was carried out from 11 April to 8 May 2010 during a non-ENSO or neutral period [*ENFEN*, 2010]. The dynamical processes driving the variability of the current system are investigated using outputs from a regional model which provides a three-dimensional view of the dynamics over a time period longer than the deployment duration. A linear *f*-plane coastal wave model is also used to provide additional information on the observed vertical structure of the near-coastal circulation.

After describing the observational data set, the model simulations and the methods used for the analysis (section 2), we present a description of the alongshore circulation and water masses observed in the region (section 3). The intraseasonal variability of the alongshore current is described using glider data and the regional model simulation (section 4). In section 5, we analyze the propagative nature of the velocity signal, and in section 6 we characterize the structure and properties of the CTW at 14°S. In section 7, we discuss the results and give concluding remarks.

2. Data and Methods

2.1. Data Sets

From 11 April to 8 May 2010, a slocum glider [*Rudnick et al*., 2004; *Testor et al*., 2010] was deployed in an active upwelling area off the Peru coast near Pisco (14°S) in order to monitor the thermohaline structure and the alongshore velocity (Figure 1). A total of 594 profiles distributed along six 100 km long cross-shore sections from the surface to a maximum depth of 1000 m were recorded. Temperature and conductivity data were collected along downward and upward profiles by an unpumped Sea-Bird CTD mounted on the glider. This CTD has a low temporal resolution (∼0.5 Hz) resulting in a typical vertical resolution of about 1–2 dbar and the data were linearly interpolated onto a regular 1 dbar vertical grid. Differences linked to thermal inertia and time responses of the sensors were observed in salinity data between neighboring upward and downward profiles. The salinity was corrected using the original conductivity time series and a temperature time series lagged with a time constant, $T_c = T - \tau_c\, \delta T/\delta t$ [*Pietri et al*., 2013]. A time lag ($\tau_c = 4.5$ s) was used to minimize differences between upward and downward consecutive profiles, which allowed to reduce the bias mainly observed in the thermocline. Note that this time lag is different than the one used in *Pietri et al*. [2013], due to the different environmental conditions and instruments.

Sea level anomalies (SLA) from satellite altimetry were used to study intraseasonal variability at 60–80 days over a time period covering the glider deployment. The SLA product consists in a daily multisatellite data gridded with a spatial resolution of 1/3° and provided by AVISO (http://www.aviso.oceanobs.com/). The SLA time series were band-pass filtered using a Gaussian window to remove variability at time scales shorter than 30 days and longer than 90 days.

Wind stress fields are provided by the Centre de Recherche et d'Exploitation Satellitaire (CERSAT, http://www.ifremer.fr/cersat/) and gridded from Metop/ASCAT measurements with a spatial resolution of 0.25° and a daily temporal resolution.

Sea surface temperature (SST) data are gridded with a resolution of 1 km from MODIS satellite data and are produced by ACRI-ST.

Currents from an eddy resolving, primitive equations, regional model were used to document the intraseasonal variability of the alongshore flow over the 2000–2006 time period. This simulation was initially performed to study the impact of coastal-trapped waves on near surface primary productivity [*Echevin et al*., 2013] using the ROMS-AGRIF (http://roms/mpl.ird.fr) version of the Regional Oceanic Modeling System (ROMS) [*Shchepetkin and McWilliams*, 2005]. The spatial resolution is 1/9° (∼12 km) and the model setting is the same as in previous similar modeling studies [*Penven et al*., 2005; *Montes et al*., 2010; *Echevin et al*., 2011]. The model bottom topography derived from the ETOPO2 database [*Smith and Sandwell*, 1983] has been smoothed in order to reduce potential error in the horizontal pressure gradient. The model possesses 32 stretched vertical sigma levels to obtain a vertical resolution ranging from 0.3 to 6.25 m for the surface layer and from 0.3 to 1086 m for the bottom layer. For a depth range between 1000 and 2400 m corresponding to the slope where the subsurface current is located, the vertical resolution in the bottom layer ranges between 160 and 350 m. As both rotation and stratification are involved in the dynamical processes related to CTW, the Burger number ($Bu = NH/fL$) is a key parameter [*Cushman-Roisin*, 1994]. The model resolution should be such that $N\,dz/f\,dx$ is of the same order of magnitude as the Burger number to describe waves that are close to geostrophic equilibrium. This leads to the relation $dz/dx \sim H/L$. With $H \sim 400$ m the thickness of the flow, and $L \sim 40$ km its width, we obtain $H/L \sim 10^{-2}$. In the depth range of the deep current, the vertical resolution is 160–350 m, thus $dz/dx \sim 1.6\text{–}3.5 \times 10^{-2}$ is close to H/L. This shows that the model discretization is adapted to describe CTW.

Three day mean temperature, salinity, velocity, and sea level from the ORCALIM ocean general circulation model at 0.25° resolution [*Garric et al*., 2008] were used to force the regional model northern, southern, and western open boundary conditions following the parameterizations of *Marchesiello et al*. [2001]. To be consistent with ORCALIM, the model was forced by daily wind stress and heat fluxes from the *European Centre for Medium-Range Weather Forecasts* (ECMWF) Integrated Forecast System (IFS, http://www.ecmwf.int/research/ifsdocs/). This simulation is referred to as REF in the following. The modeled SLA was band-pass filtered similarly to the satellite altimetry data. In the following, SLA refers to band-pass filtered SLA.

2.2. Observed and Modeled Alongshore Currents

Geostrophic velocities perpendicular to the glider track were computed using the density field from the glider measurements and thermal wind balance as in *Pietri et al*. [2013]. Along the glider section, the Coriolis parameter is $f \sim -3.6 \times 10^{-5}\ s^{-1}$ and the average Brunt-Väisälä frequency reaches $2.5 \times 10^{-4}\ s^{-2}$ in the thermocline. In this near-coastal region, the Rossby radius is of ∼20 km, thus in order to get a geostrophically balanced density field, the high-resolution in situ data were filtered using a triangular moving average of ∼20 km (∼24 h at the glider's speed). The relatively short Rossby radius compared to values (∼50–100 km) previously reported in the literature [*Smith*, 1978; *Penven et al*., 2005] is not properly resolved by the present model. This incites us to perform future studies with an enhanced horizontal (e.g., 7.5 km as in *Colas et al*. [2008, 2012] or less) and potentially vertical resolution. This is underway and will be published in future work.

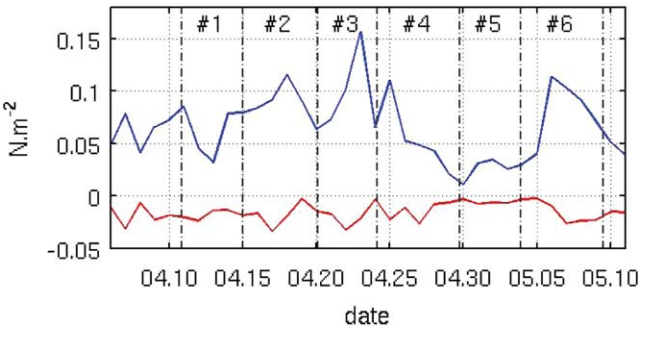

Figure 2. Time evolution of the wind stress alongshore (blue line) and cross-shore (red line) components (in N m^{-2}) near 14°S, 77°W from ASCAT scatterometer during the glider deployment. The dates corresponding to each glider cross-shore section are marked by dashed vertical lines.

The constraint of specifying a level of no motion is relaxed as the depth-averaged velocity measured by the glider between two surfacings, computed from the difference between underwater dead reckoning and GPS fixes at the surface, can be used. Surface ageostrophic circulation in the alongshore direction is assumed to be weak since the Ekman transport is mostly cross-shore (Figure 2). Assuming also that the ageostrophic flow is weak below the Ekman layer, the filtered depth-averaged velocity provides

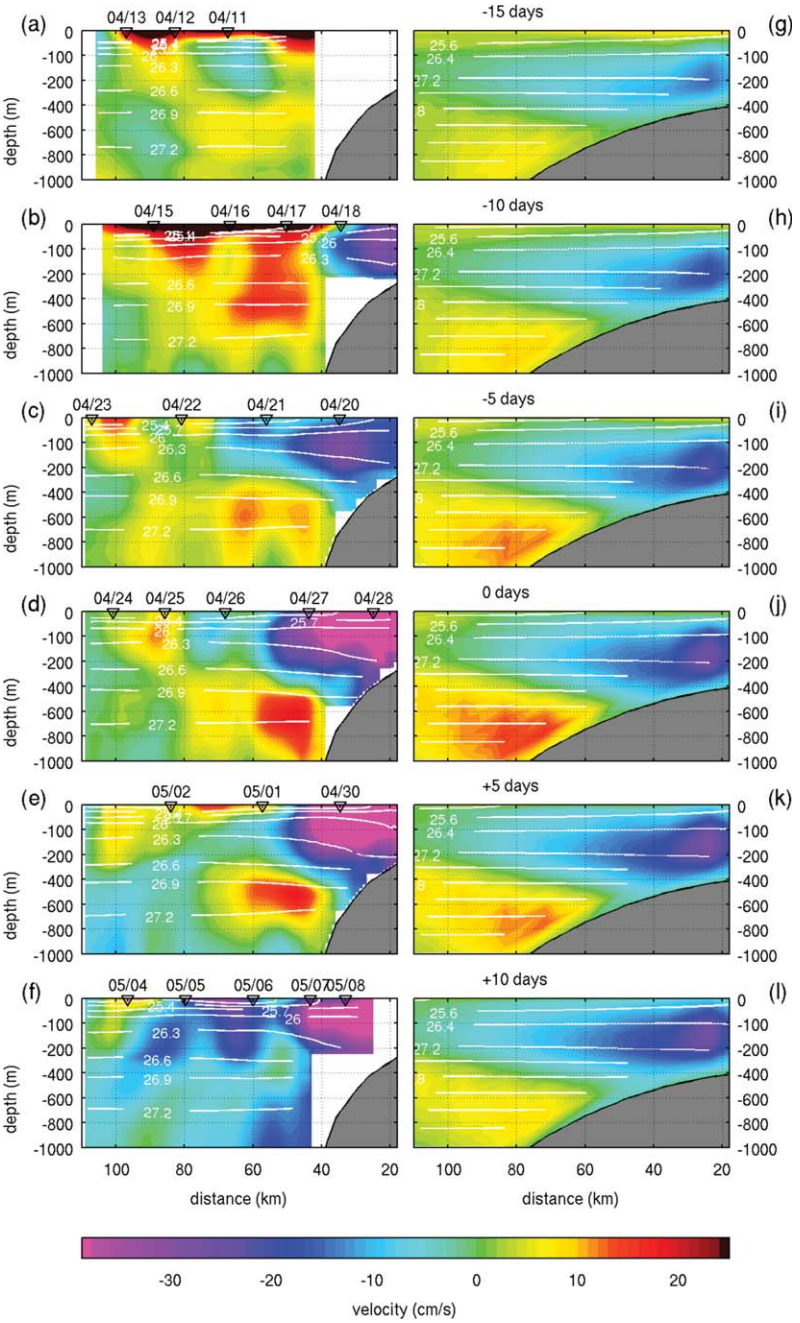

Figure 3. (a–f) Alongshore geostrophic velocity near 14°S (perpendicular to each glider sections) objectively mapped. White lines represent the isopycnals of the original data. (g–l) Alongshore velocity composite from the regional model simulation at 14°S. The criteria used to build the composite are detailed in section 2. White lines represent the isopycnals. The depth axis is not linear in order to highlight the top 200 m of the sections. The horizontal axis represents the distance from the coast.

a robust estimate of the depth-averaged absolute geostrophic flow, as shown in a previous study [*Pietri et al.*, 2013] where glider-derived geostrophic current and Acoustic Doppler Current Profiler (ADCP) measurements showed a relatively good agreement (with a maximum error of 4 cm s^{-1}).

Note that the glider was equipped with an altimeter that was unfortunately defective during part of the mission. For visualization purposes (see Figure 3), the data were objectively mapped above the slope and close to the sea floor using a decorrelation scale of 30 km in the horizontal and 200 m in the vertical.

In order to investigate the three-dimensional structure and the forcing responsible for the observed alongshore current, the model simulation is used to construct composite fields having characteristics similar to

those observed. Events exhibiting a local maximum in equatorward velocity (at 14°S), within 40 km from the slope and at ~700 m deep, higher than 5 cm s^{-1} and a poleward velocity, at 100 m depth within 60 km from the slope, also higher than 5 cm s^{-1} were selected. A composite field was then constructed by averaging 16 such events selected in the simulation. A composite temporal event was also created by averaging model fields 60 days before and after each selected event. Using this method, the temporal evolution of the alongshore current can be studied over a time period of 120 days, centered on the peak of deep equatorward flow.

3. Results

3.1. Alongshore Circulation

Figures 3a–3f display the cross-shore structure of the alongshore current and its temporal evolution. From 10 to 19 April, a strong equatorward surface flow with a surface maximum velocity of ~30 cm s^{-1} associated with the PCC is observed offshore of 40 km (Figures 3a and 3b). From 10 to 14 April, this current is composed of two cores, the nearshore one extending vertically up to ~50 m depth while the offshore one located near ~90 km extends up to ~200 m depth (Figure 3a). In contrast, from 14 to 18 April, equatorward velocities of ~15 cm s^{-1} are observed at depths ranging ~600 m (Figure 3b). After 19 April, the PCC is much less visible. This is associated with a ~100 km displacement of the upwelling front offshore of the glider section from 15 to 25 April, as seen in SST maps (Figure 1).

Between 17 April and 8 May, poleward velocities associated with a surfacing PCUC are observed above the continental slope. Around 18 April (Figure 3b) the PCUC is confined within ~40 km from the shore with a maximum velocity of ~25 cm s^{-1}. Then from 19 April to 1 May (Figures 3c–3e), the PCUC intensifies and broadens, extending up to ~60 km from the shore and reaching ~40 cm s^{-1} and a vertical extent of ~300 m. During the last part of the mission from 4 May to 8 May (Figure 3f), poleward velocities occupy the section from the shore up to ~90 km, and display a nearshore and an offshore surface core.

Between 26 and 29 April (Figure 3d), the PCUC transport reaches a maximum value of 5 ± 0.8 Sv in the 0–600 m layer and within 80 km from the shore. Using recent ADCP measurements acquired along the Peruvian coast from 2008 to 2012, *Chaigneau et al*. [2013] estimated an averaged PCUC transport of ~4–5 Sv at 14°S. Note that their results show a weaker (10 cm s^{-1}) and deeper PCUC with larger horizontal and vertical extensions.

Below the PCUC, our measurements reveal intense equatorward subsurface velocities from 10 April to 2 May (Figures 3a–3e) related to the CPDCC [*Chaigneau et al*., 2013]. The flow at ~600 m depth intensifies from 10 April (~8 cm $s^{-1)}$ to 27 April (~15 cm s^{-1}). When the current is strongest it reaches a width of ~40 km and a vertical extension of ~700 m, from 300 to 1000 m depth. After 27 April, the current weakens and the velocity decreases. At its peak in 25–28 April, this deep coastal current transports up to 2.5 ± 0.1 Sv in the 200–1000 m layer and within 90 km from the shore (Figure 3d).

3.2. Water Masses

Contrasted water masses were observed along the glider section (Figure 4). The Cold Coastal Water (CCW) [*Zuta et al*., 1978] is a cool (14–16°C) and salty (35–35.1) water mass transported by the PCUC and upwelled at the coast. The Subtropical Surface Water (STSW) *Wyrtki* [1967] characterized by relatively high temperature (16–18°C) and salinity (35–35.1) is located in the surface layer offshore of the CCW. The Eastern South Pacific Intermediate Water (ESPIW) [*Schneider et al*., 2003], a fresher water (34.7–34.9) with temperature from 13°C to 16°C originating from the South is located just below the thermocline and at ~100 km from the shore. At greater depth than 500 m lies a much fresher (34.5–34.6) and colder (4–7°C) water mass, the Antarctic Intermediate Water (AAIW) [*Reid*, 1965], which is transported equatorward by the CPDCC (Figure 4a).

4. Intraseasonal Variability

The measurements presented here are the first glider-based high-resolution observations of deep coastal equatorward velocities along the Peru coast. Intermittent equatorward velocities at a period of 40–60 days and at 735 m depth have also been observed further South (30°S) from a currentmeter moored off the

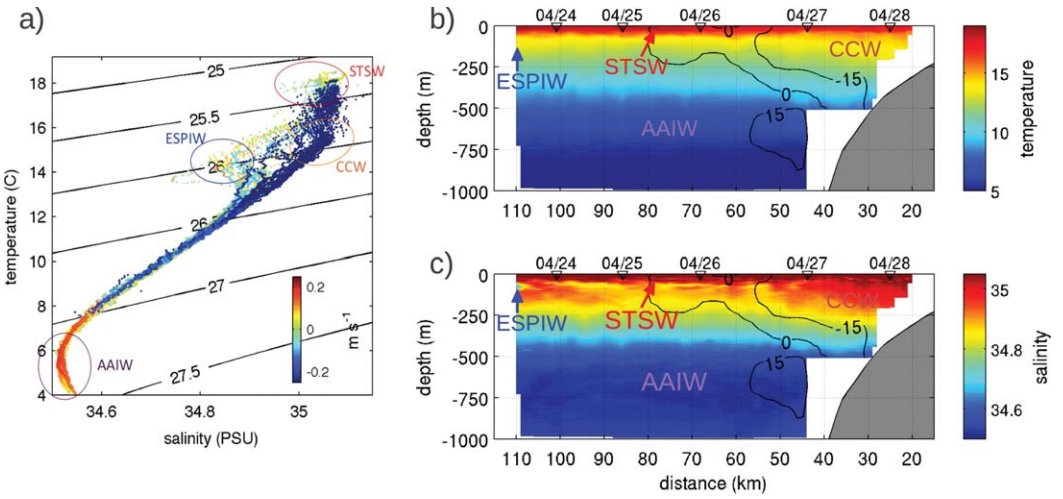

Figure 4. (a) θ-S diagram from the glider data (from 24 to 28 April 2010). Color coding indicates the alongshore velocity (positive equatorward). Water masses are indicated by colored circles. (b) Salinity and (c) temperature from the fourth section of the glider deployment (at 14°S) and the location of the different water masses are indicated. Black contours represent the alongshore velocity (in cm s^{-1}) from the fourth glider section.

Chilean coast [*Shaffer et al*., 1997]. Similar events have been reported in the California Current System by *Kosro* [2002]. Using ADCP transects between 38°N and 44°N, this author showed that an equatorward current with velocities exceeding 20 cm s^{-1} was trapped near the bottom at ~300 m depth in November 1997 and February 1998, during the strong 1997–1998 El Niño event. Model studies also suggest the existence of a deep equatorward coastal flow off Peru. *Colas et al*. [2008] gave evidence of an equatorward coastal current at 400 m depth with velocity higher than 10 cm s^{-1} during the 1997–1998 El Niño. Besides, *Montes et al*. [2010] identified a mean sluggish equatorward flow of ~2 cm s^{-1} underneath the PCUC, between 300 m deep and 1500 m deep.

In order to provide further insight on the temporal variability of the coastal circulation, we investigate model events showing alongshore velocities similar to the observed, following the criteria defined in section 2. Figures 3g–3l display sections of the alongshore velocity of the composite event at 14°S. Its temporal evolution is shown before and after the occurrence of maximum deep equatorward flow (time $t = 0$ corresponds to the maximum velocity at 700 m). Note that the shelf and slope are quite different from the observed ones, indeed the model bottom topography is smoothed to minimize potential errors in the horizontal pressure gradient. Figure 5 displays the standard deviation associated with the composite at $t = 0$ days. An equatorward surface current of ~5 cm s^{-1} can be observed during 30 days. At $t = -15$ days (Figure 3g), it is ~140 km wide and close to the coast while 15 days later it is located ~100 km offshore. This current resembles the observed PCC albeit much weaker (~5 cm s^{-1} versus ~30 cm s^{-1} in the glider observations). Interestingly, it moves offshore ~10 days before the occurrence of the maximum deep equatorward flow, as in the observed sections. Note that this surface current presents a strong variability in the ensemble of selected events, as the associated standard deviation is ~10 cm s^{-1} (Figure 5), thus higher than the mean. Close to the coast, a strong surfacing poleward current can be observed. It has a vertical extent of ~250 m and a width of ~60 km. Its velocity increases from ~5 cm s^{-1} ($t = -15$ days, Figure 3g) to ~20 cm s^{-1} ($t = 0$ days, Figure 3j). This current is quite similar to the observed PCUC, albeit slightly

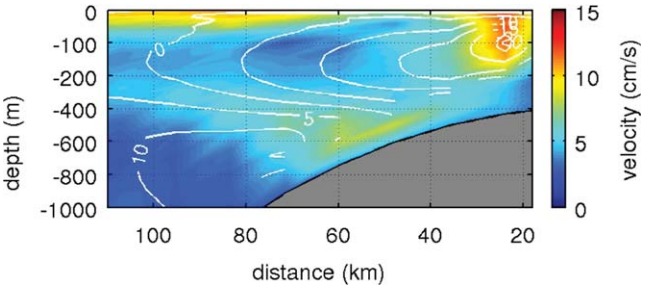

Figure 5. Vertical section (at 14°S) of the standard deviation associated with the model composite at $t = 0$ days. White lines represent the alongshore velocities from the composite at $t = 0$ days.

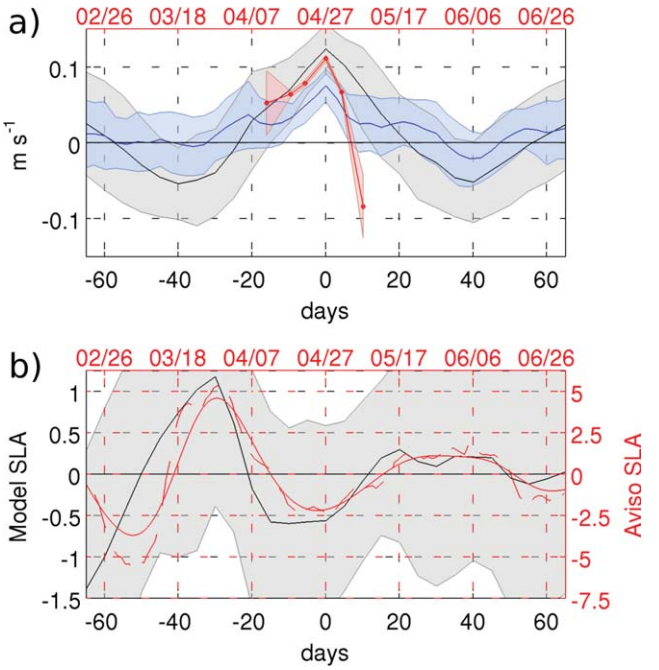

Figure 6. (a) Temporal evolution of the deep alongshore coastal velocity at 14°S (in m s^{-1}) for the modeled composite event. The black (respectively, blue) line marks the velocity at 700 m depth of the mean REF (respectively, OBCsim) composite event while the light gray (respectively, blue) envelope marks the ensemble selected events. The glider alongshore coastal geostrophic velocity at 14°S and 700 m deep is marked by a red line and red diamonds. Red envelope corresponds to errors due to the optimal interpolation. (b) Same as Figure 6a but for sea level anomalies (SLA, in m). The red line marks the SLA from AVISO data and the black line from the REF composite (the OBCsim composite SLA is not shown). The red dashed line marks the SLA only high pass filtered for frequencies below 1/(90 days). Note the change of scale between the AVISO and model composite SLA.

wider and weaker. The variability of the PCUC surfacing core is high in the model ensemble, reaching ∼10–15 cm s^{-1} at $t = 0$ days in the upper 150 m of the water column (Figure 5).

A remarkable result from the model is the presence of a deep equatorward current, with a vertical structure and time variability similar to the one observed. At $t = -15$ days, it is confined within ∼40 km from the continental slope, then its width increases during 15 days, reaching ∼80 km. The vertical extent of this current is ∼1000 m, between ∼400 and ∼1400 m depth. Equatorward velocity at ∼700 m depth increases (Figures 3g–3i), reaches a maximum of ∼15 cm s^{-1} ($t = 0$, Figure 3j) and decreases (Figures 3k–3l), in a very similar way as observed with the glider. The differences between model results and our observations are likely linked with the mesoscale structures present in the glider sections and partly filtered in the model composite.

The temporal evolution of the deep coastal alongshore velocity is now examined in more detail. Figure 6a displays the time series of the glider and model composite subsurface velocities. Glider velocities and composite velocities at 700 m depth are averaged between the shore and 30 km offshore. The model velocity at depth alternate between positive and negative velocities with a period of ∼70 days. Even though the duration of the glider mission is relatively short with respect to this time scale, observed and composite velocities show a relatively good agreement. Note that the observed velocity between 6 and 8 May differs more from the composite velocity than at other dates. During this particular period the glider did not record data close to the coast, so that the velocity in that location is extrapolated using objective mapping. Overall, the consistency between the observations and the model composite suggest that the observed variability could be related to an intraseasonal event with a time scale of ∼60–70 days.

Figure 6b displays the time series of AVISO coastal SLA at 14°S from 21 February to 1 July 2010 along with the SLA composite event from the model simulations. The observed and model time series show an in-phase alternation of negative and positive anomalies, with a positive peak near $t \sim -30$ days and a weaker variability after $t = 0$. Note that the range of SLA variability in the model composite events is much lower than in altimetry data, mainly because composite events are created by averaging several model fields. Nevertheless, the similar temporal variability in the model and observations for the deep current and for sea level reinforces our hypothesis that the same type of intraseasonal event is seen in the observations and in the model composites.

5. Propagation Along the Coast

The spatiotemporal structure of the model composite event is now examined. Figure 7 displays horizontal sections of the meridional velocity at 700 m depth. The velocity fields display nearshore positive and

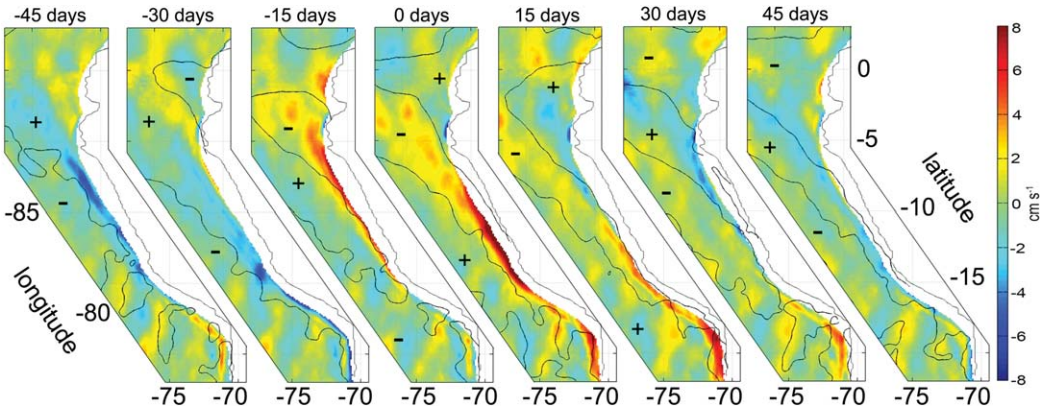

Figure 7. Meridional velocity (in m s^{-1}, color coding) at 700 m depth and sea level anomaly (in cm, black contour corresponds to 0 cm) from the regional model composite event (REF simulation). (+) and (−) labels indicate a sea level anomaly, respectively, positive and negative.

negative velocity patterns of $\pm$10 cm s^{-1}, alternating with a time period of $\sim$70 days. These coastal-trapped patterns clearly propagate poleward from 5°S to 20°S. As they seem to originate from the equatorial region, they are likely the signature of CTW forced by eastward propagating IEKW [*Brink*, 1982; *Romea and Smith*, 1983; *Clarke and Ahmed*, 1999; *Hormazabal et al*., 2002]. Note also the westward propagation of the sea level and velocity anomalies in the 0°S–10°S latitudinal band, corresponding to the Rossby waves forced by CTW [e.g., *Belmadani et al*., 2012; *Bonhomme et al*., 2007].

As the alongshore velocity signal seems to propagate poleward from the equator, the correlation of lagged time series of subsurface alongshore velocity for the whole simulation has been estimated. The time lag at which maximum correlation between distant pairs of coastal alongshore velocity (at 700 m depth and from 5°S to 22°S) is obtained gives an estimation of the propagation speed of CTW. The mean poleward propagation speed is then $\sim 1.2 \pm 0.4$ m s^{-1}.

These results suggest that the variability of the CPDCC observed by the glider at 14°S could be associated with the passage of a CTW forced in the equatorial region.

6. Coastal-Trapped Wave Characteristics

In order to further investigate the characteristics of CTW which may propagate near 14°S during the period of study, the vertical structure of the alongshore flow and propagation speed of coastal modes were calculated using an *f*-plane, linear, coastal-trapped wave model [*Brink and Chapman*, 1987]. The bottom topography along the 14°S section and the mean stratification from the glider measurements were used to find the CTW vertical modes at time scales of 60–70 days. The shelf slope width is 85 km and bottom depth is kept constant offshore at 4000 m depth. A mean squared Brunt-Väisälä frequency profile, N^2, is defined by averaging glider density profiles offshore of 80 km and completed below 1000 m by an exponential tail [*Romea and Smith*, 1983].

Three coastal modes are obtained. The first mode (figure not shown) presents a zero crossover for alongshore velocity at $\sim$1800 m deep and a propagation speed of $\sim$3.1 m s^{-1}. The alongshore flow associated with this mode vertical structure is thus very different from the observed, and propagates much faster than the CTW identified in the regional model simulation. Figure 8 displays the alongshore velocity structure from the CTW second and third modes. The second mode presents zero crossovers at $\sim$500 and $\sim$2700 m deep (Figure 8b) and a propagation speed of $\sim$1.7 m s^{-1}. The third mode has zero crossovers at $\sim$200, $\sim$1300, and $\sim$3200 m deep (Figure 8c) and a propagation speed of $\sim$1.1 m s^{-1}. For each mode, a scale factor was computed to minimize the difference between glider velocity (between 26 and 28 April, Figure 3d) and the CTW velocity structure, for a vertical profile located at less than 15 km from the slope. These CTW alongshore velocity structures also display a deep equatorward anomaly, trapped within 50–70 km from the continental slope, a structure which strongly resembles the one shown in Figure 3. Furthermore, the propagation speeds of these modes are close to the one estimated from the regional model deep current

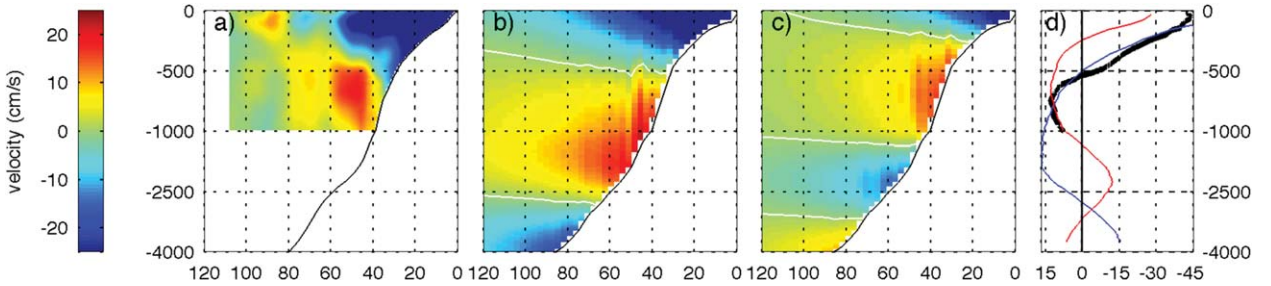

Figure 8. Alongshore velocity (in cm s^{-1}) from (a) the 23–28 April glider section; (b) from the second; and (c) third CTW baroclinic modes resulting from the *Brink and Chapman* [1987] *f*-plane, linear model. (d) Coastal velocity profiles (within 15 km from the slope) from the glider section (bold black line) and from the second (blue line) and third (red line) CTW baroclinic modes. Note that both CTW modes have been multiplied by a scaling factor as to minimize the difference with the glider velocities.

lagged time series. Overall, these results suggest that the observed alongshore velocity vertical structure could result from a linear combination of the second and third CTW modes.

Note that *Clarke and Ahmed* [1999] also found a vertical velocity structure close to the observed using a more complex linear wave model taking into account planetary β effect and bottom friction. In their model, the alongshore flow is forced by an EIKW first baroclinic mode, and without wind. Their results showed a subsurface equatorward jet with a core at ~500 m depth and a maximum velocity of ~14–16 cm s^{-1} trapped along the continental slope (see their Figure 14a). Furthermore, this velocity structure is present along the coast from 11°S to 35°S and deepens southward, which supports the idea that this current may be found all along the coasts of Peru and Chile [*Shaffer et al*., 1997].

7. Discussion and Conclusions

Repeated high-resolution cross-shore sections off Peru (14°S) during April–May 2010 allowed to document the complex vertical structure of the coastal current system with a focus on the PCUC and the CPDCC, and describe their variability over the studied period. First, the poleward PCUC, reached the surface during at least 1 month, exhibiting velocities as high as 35 cm s^{-1}. Second, the thermal front and associated surface equatorward jet were displaced offshore by ~100 km. Third, a coastal, deep equatorward current reaching up to 15 cm s^{-1} and transporting up to 2.5 Sv was observed within 70 km from the shelf and between 300 and 1000 m depth. Two different models were used to provide insight on the dynamical processes responsible for the observed flow and on its three-dimensional structure. Simulations from a three-dimensional regional model showed that the current structure is likely associated with the propagation of a CTW at a time scale of ~60–70 days. High order vertical modes from a linear CTW model show alongshore velocity patterns similar to the observed.

Different forcings are known to generate CTW. Remotely forced, eastward propagating Equatorial Kelvin waves may trigger CTW upon their reaching the South American coasts [*Smith*, 1978; *Romea and Smith*, 1983; *Clarke and Shi*, 1991; *Belmadani et al*., 2012]. CTW can also be generated by local winds that create sea level anomalies propagating poleward along the coast [*Battisti and Hickey*, 1984; *Brink*, 1991]. We now investigate whether the wind forcing may have played such a role in the present case study.

During the glider deployment the local wind was strongly variable (Figure 2). From 11 to 14 April, relaxation of the wind stress could explain the observed warmer surface temperature (Figure 1a). Then the alongshore wind stress increased from 15 to 22 April, followed by a temperature drop of 4°C from 21 April and an offshore displacement of the PCC (Figures 3b–3c). These modifications of the surface circulation and thermal conditions are consistent with those generated by a wind-driven upwelling event. However, from 23 to 30 April, the wind stress decreased significantly while the equatorward jet remained offshore and the coastal temperature did not rise, suggesting that other processes than wind-driven upwelling may occur during the end of the glider cruise.

To further evaluate the respective influence of local wind and EIKW forcing in the model, two sensitivity simulations with a setting similar to the reference simulation (hereafter REF) described in section 2.1 but

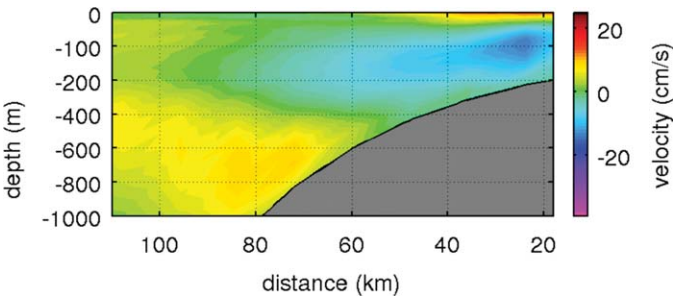

Figure 9. Alongshore velocity composite (at $t = 0$ days) from the regional model simulation OBCsim at 14°S. The criteria used to build the composite are detailed section 2. The depth axis is not linear in order to highlight the top 200 m of the section. The horizontal axis represents the distance from the coast. The colorscale is the same as in Figure 3.

with a different wind forcing and open boundary conditions were compared [see also *Echevin et al*. [2013].

The Qsim simulation was forced with the same 3 day mean interannual open boundary conditions as in the reference simulation, but with a slightly different wind forcing (daily Quickscat data instead of daily ECMWF data). Note that the ECMWF IFS model assimilates Quikscat data, so that the two products should not be very different. The criteria used to select CTW events in the model and described in section 2.2 were applied to this simulation. Qsim presented about the same number of CTW events (15) over 2000–2006, with 10 events happening at approximately the same dates (within a 10 day interval) as in REF. This shows that the generation of CTW is robust in our model, and not very sensitive to the choice of wind forcing. Interestingly, the CTW propagation velocity obtained from lag correlation of the deep current time series (see section 5) was larger (1.6 ± 0.4 m s^{-1}) in Qsim than in REF (1.2 ± 0.4 m s^{-1}). Modal decomposition of the REF and Qsim solutions at 14°S (figures not shown) performed using the *Brink and Chapman* [1987] model showed that the vertical structures of the different modes resemble the ones obtained using the glider data (Figure 8). Furthermore, the propagation speed of the second mode is 1.1 m s^{-1} in REF and 1.4 m s^{-1} in Qsim. These values are thus close to the propagation speeds obtained from lag correlation. This clearly illustrates that the wind forcing, likely its mean structure, impacts the mean density field and thus modifies the speed of CTW modes.

As shown previously, model results (REF experiment) suggest that the observed structure in the alongshore current may be the signature of a CTW of equatorial origin (Figure 7). This is consistent with results from *Romea and Smith* [1983], who analyzed sea level variations from coastal stations and moored currentmeters. They found evidence of a first mode baroclinic coastal Kelvin wave propagating between 2°S and 17°S along the Peru coast and reported tenuous evidence of equatorial forcing of the latter from the near-equatorial Galapagos region. To confirm our findings, a second sensitivity simulation was performed by damping the EIKW coming from the western boundary into the model domain. This simulation (OBCsim) was forced by daily ECMWF wind (as in REF) and monthly climatological open boundary conditions, which allows to filter intraseasonal EIKW [see *Echevin et al*., 2013]. OBCsim presented less CTW events (10) than REF and only 3 of them took place at the same dates as in REF, suggesting that most of CTW events in REF were forced by the equatorial boundary forcing. A section of the alongshore velocity from the OBCsim composite event at 14°S (Figure 9) shows features comparable to those of REF (Figure 3j). The CPDCC and PCUC occupy the same depth and cross-shore range than in REF but their intensities are reduced (Figure 6a). Note also that the surface PCC is trapped at the coast, which contrasts with the observations and the REF composite. The OBCsim experiment shows that the wind forcing is able to generate CTW of modal structure superior to one. This contrasts with results from other upwelling regions, as e.g., the coast of Oregon, where *Battisti and Hickey* [1984] showed that local wind was mostly generating waves associated with a first mode. In conclusion, it is likely that the observed structure results from the propagation of a disturbance of equatorial origin rather than from the local wind forcing. However, a dedicated numerical experiment using realistic wind and IEKW boundary forcing for the April–May 2010 time period would be necessary to ascertain the origin of the observed CTW forcing. This is beyond the scope of the present study and is reserved for future work.

In conclusion, CTW may modulate the variability of the deep equatorward flow off Peru at intraseasonal time scales, thus potentially influencing the transport of intermediate water of Antarctic/Subantarctic origin to tropical regions. However, the veracity of this slow advective process will need to be confirmed using

pluriannual glider repeat sections along with realistic, high-resolution regional model simulations covering several decades.

Acknowledgments
The authors wish to thank X. Carton and F. Durand for constructive and helpful discussions. We also thank the technical staff of IMARPE and the DT-INSU for logistic and technical support. Financial support was provided by EGO-COST Action ES0904, FP7 EU project JERICO, and the Peru Ecosystem Projection Scenarios (PEPS) ANR-VMCS-2008 project. ROMS model simulations were computed using the NEC-SX8 Brodie, IBM cluster Vargas, and Ada supercomputers from IDRIS (http://www.idris.fr/) and the PC cluster network from LOCEAN. A. Pietri and A. Albert were funded by a scholarship of the French Ministre de l'Education et de la Recherche. This work was also supported by the IRD-IMARPE DISCOH Joint International Laboratory and CNRS-INSU. Support from the TOSCA/CNES project "Variabilité du niveau de la mer, vents et circulation de surface dans la zone côtière de l'upwelling péruvien" is also acknowledged.

References

Albert, A., V. Echevin, M. Lévy, and O. Aumont (2010), Impact of nearshore wind stress curl on coastal circulation and primary productivity in the Peru upwelling system, *J. Geophys. Res.*, *115*, C12033, doi:10.1029/2010JC006569.

Battisti, D. S., and B. M. Hickey (1984), Application of remote wind-forced coastal trapped wave theory to the Oregon and Washington Coasts, *J. Phys. Oceanogr.*, *14*, 887–903, doi:10.1175/1520-0485(1984)014.

Belmadani, A., V. Echevin, B. Dewitte, and F. Colas (2012), Equatorially-forced intraseasonal propagations along the Peru-Chile coast and their relation with the nearshore eddy activity in 1992-2000: A modelling study, *J. Geophys. Res.*, *117*, C04025, doi:10.1029/2011JC007848.

Bonhomme, C., O. Aumont, and V. Echevin, (2007), Advective transport caused by intraseasonal Rossby waves: A key player of the high chlorophyll variability off the Peru upwelling region, *J. Geophys. Res.*, *112*, C09018, doi:10.1029/2006JC004022.

Brink, K. H. (1982), A comparison of long coastal trapped wave theory with observations off Peru, *J. Phys. Oceanogr.*, *12*, 897–913.

Brink, K. H. (1991), Coastal-trapped waves and wind-driven currents over the continental shelf, *Ann. Rev. Fluid Mech.*, *23*, 389–412.

Brink, K. H., and D. C. Chapman (1987), Programs for computing properties of coastal-trapped waves and wind-driven motions over the continental shelf and slope, *Tech. Rep., WHOI-87-24*, 122 pp., Woods Hole Oceanogr. Inst., Woods Hole, Mass.

Brink, K. H., J. S. Allen, and R. L. Smith (1978), A study of low-frequency fluctuations near the Peru coast, *J. Phys. Oceanogr.*, *8*(6), 1025–1041.

Brink, K. H., D. Halpern, A. Huyer, and R. L. Smith (1983), The physical environment of the Peruvian upwelling system, *Prog. Oceanogr.*, *12*, 285–305.

Chaigneau, A., N. Dominguez, G. Eldin, L. Vasquez, R. Flores, C. Grados, and V. Echevin (2013), Near-coastal circulation in the Northern Humboldt Current System from shipboard ADCP data, *J. Geophys. Res.*, *118*, 5251–5266, doi:10.1002/jgrc.20328.

Clarke, A. J., and C. Shi (1991), Critical frequencies at ocean boundaries, *J. Geophys. Res.*, *96*, 10,731–10,738.

Clarke, A. J., and R. Ahmed (1999), Dynamics of remotely forced intraseasonal oscillations off the western coast of South America, *J. Phys. Oceanogr.*, *29*, 240–258.

Colas, F., X. Capet, J. McWilliams, and A. Shchepetkin (2008), 1997–1998 El Niño off Peru: A numerical study, *Prog. Oceanogr.*, *79*, 138–155.

Colas, F., J. McWilliams, X. Capet, and J. Kurian (2012), Heat balance and eddies in the Peru-Chile current system, *Clim. Dyn.*, *39*, 509–529.

Cravatte, S., J. Picaut, and G. Eldin (2003), First and second baroclinic Kelvin modes in the equatorial Pacific at intraseasonal timescales, *J. Geophys. Res.*, *108*, 3266, doi:10.1029/2002JC001511.

Cushman-Roisin, B. (1994), *Introduction to Geophysical Fluid Dynamics*, 320 pp., Prentice Hall, New York.

Dewitte, B., S. Illig, L. Renault, K. Goubanova, K. Takahashi, D. Gushchina, K. Mosquera, and S. Purca (2011), Modes of covariability between sea surface temperature and wind stress intraseasonal anomalies along the coast of Peru from satellite observations (2000–2008), *J. Geophys. Res.*, *113*, C04028, doi:10.1029/2010JC006495.

Echevin, V., F. Colas, A. Chaigneau, and P. Penven (2011), Sensitivity of the northern Humboldt current system nearshore modeled circulation to initial and boundary conditions, *J. Geophys. Res.*, *116*, C07002, doi:10.1029/2010JC006684.

Echevin, V., A. Albert, M. Lévy, M. Graco, O. Aumont, A. Pietri, and G. Garric (2013), Intraseasonal variability of nearshore productivity in the Northern Humboldt Current System: The role of coastal trapped waves, *Cont. Shelf Res.*, *73*, 14–30, doi:10.1016/j.csr.2013.11.015.

ENFEN (2010), Informe técnico no. 04-2010, *Comité Multisectorial encargado del Estudio Nacional del Fenómeno El Niño*, Lima, Peru. [Available at http://www.imarpe.gob.pe/imarpe/archivos/informes/imarpe_inftco_inf_tecnico_2010_04.pdf.]

Garric, G., R. Bourdalle-Badie, O. Le Galloudec, C. Bricaud, C. Derval, E. Durand, and Y. Drillet (2008), Description of the interannual experiment ORCA025-t09, 1998-2006, *Annex 2 of Mercator Ocean Rep., 235*, 32 pp.

Hormazabal, S., G. Shaffer, J. Letelier, and O. Ulloa (2001), Local and remote forcing of sea surface temperature in the coastal upwelling system off Chile, *J. Geophys. Res.*, *106*(C8), 16,657–16,671.

Hormazabal, S., G. Shaffer, and O. Pizarro (2002), Tropical Pacific control of intraseasonal oscillations off Chile by way of oceanic and atmospheric pathways, *Geophys. Res. Lett.*, *29*(6), 1081, doi:10.1029/2001GL013481.

Huyer, A. (1980), The offshore structure and subsurface expression of sea level variations off Peru, 1976-1977, *J. Phys. Oceanogr.*, *10*, 1755–1768.

Huyer, A., M. Knoll, T. Paluskiewicz, and R. L. Smith (1991), The Peru undercurrent: A study in variability, *Deep Sea Res., Part A, 38*, suppl. 1, S247–S271.

Kosro, P. M. (2002), A poleward jet and an equatorward undercurrent observed off Oregon and northern California, during the 1997-98 El Niño, *Prog. Oceanogr.*, *54*, 343–360.

Marchesiello, P., J. C. McWilliams, and A. Shchepetkin (2001), Open boundary conditions for long-term integration of regional oceanic models, *Ocean Modell.*, *3*, 1–20.

Marchesiello, P., J. C. McWilliams, and A. Shchepetkin (2003), Equilibrium structure and dynamics of the California current system, *J. Phys. Oceanogr.*, *33*, 753–783.

Montes, I., F. Colas, X. Capet, and W. Schneider (2010), On the pathways of the equatorial subsurface currents in the eastern equatorial Pacific and their contributions to the Peru-Chile undercurrent, *J. Geophys. Res.*, *115*, C09003, doi:10.1029/2009JC005710.

Montes, I., W. Schneider, F. Colas, B. Blanke, and V. Echevin (2011), Subsurface connections in the eastern tropical Pacific during La Niña 1999-2001 and El Niño 2002-2003, *J. Geophys. Res.*, *116*, C12022, doi:10.1029/2011JC007624.

Penven, P., V. Echevin, J. Pasapera, F. Colas, and J. Tam (2005), Average circulation, seasonal cycle, and mesoscale dynamics of the Peru Current System: A modeling approach, *J. Geophys. Res.*, *110*, C10021, doi:10.1029/2005JC002945.

Pietri, A., P. Testor, V. Echevin, A. Chaigneau, L. Mortier, G. Eldin, and C. Grados (2013), Finescale vertical structure of the upwelling system off Southern Peru as observed from glider data, *J. Phys. Oceanogr.*, *43*, 631–646, doi:10.1175/JPO-D-12-035.1.

Reid, J. L. (1965), *Intermediate Waters of the Pacific Ocean*, vol. 2, 85 pp., Johns Hopkins Univ. Press, Baltimore, Md.

Romea, R. D., and R. L. Smith (1983), Further evidence for coastal trapped waves along the Peru coast, *J. Phys. Oceanogr.*, *13*, 1341–1356.

Rudnick, D. L., R. E. Davis, C. C. Eriksen, D. M. Fratantoni, and M. J. Perry (2004), Underwater gliders for ocean research, *Mar. Technol. J.*, *38*(1), 48–59.

Schneider, W., R. Fuenzalida, E. Rodriguez-Rubio, and J. Garcés-Vargas (2003), Characteristics and formation of eastern South Pacific intermediate water, *Geophys. Res. Lett.*, *30*(11), 1581, doi:10.1029/2003GL017086.

Shaffer, G., O. Pizarro, L. Djurfeldt, S. Salinas, and J. Rutllant (1997), Circulation and low-frequency variability near the Chilean coast: Remotely forced fluctuations during the 1991-92 El Niño, *J. Phys. Oceanogr.*, *27*, 217–235.

Shchepetkin, A. F., and J. C. McWilliams (2005), The regional oceanic modeling system (ROMS): A split-explicit, free-surface, topography-following coordinate oceanic model, *Ocean Modell.*, *9*, 347–404, doi:10.1016/j.ocemod.2004.08.002.

Smith, R. L. (1978), Poleward propagating perturbations in currents and sea levels along the Peru Coast, *J. Geophys. Res.*, *83*(C12), 6083–6092.

Smith, W. H. F., and D. T. Sandwell (1997), Global seafloor topography from satellite altimetry and ship depth soundings, *Science*, *277*, 1957–1962.

Strub, P., J. Mesias, V. Montecino, J. Ruttlant, and S. Salinas (1998), Coastal ocean circulation off western South America, in *The Sea, The Global Coastal Ocean*, vol. 11, edited by A. Robinson and K. Brink, pp. 273–313, John Wiley, New York.

Testor, P., et al. (2010), Gliders as a component of future observing systems, in *Proceedings of OceanObs'09: Sustained Ocean Observations and Information for Society*, vol. 2, edited by J. Hall, D. E. Harrison, and D. Stammer, ESA Publ. WPP-306, Venice, Italy, doi:10.5270/OceanObs09.cwp.89.

Wyrtki, K. (1966), Oceanography of the eastern equatorial Pacific Ocean, *Mar. Biol. Ann. Rev.*, *4*, 33–68.

Wyrtki, K. (1967), Circulation and water masses in the eastern equatorial Pacific Ocean, *J. Oceanol. Limnol.*, *1*, 117–147.

Zuta, S., T. Rivera, and A. Bustamante (1978), Hydrologic aspects of the main upwelling areas off Peru, in *Upwelling Ecosystems*, edited by R. Boje and M. Tomczak, pp. 235–257, Springer, Berlin.

Erratum

In the originally published version of this article, a decimal point was missing in a measurement. In section 2.1, (~5 Hz) has been corrected to (~0.5 Hz). This version may be considered the authoritative version of record.